



**CHALMERS**  
UNIVERSITY OF TECHNOLOGY

## **Complete precipitate dissolution during adiabatic shear localisation in a Ni-based superalloy**

Downloaded from: <https://research.chalmers.se>, 2021-08-31 10:59 UTC

Citation for the original published paper (version of record):

Hörnqvist Colliander, M., Sundell, G., Thuvander, M. (2020)

Complete precipitate dissolution during adiabatic shear localisation in a Ni-based superalloy

Philosophical Magazine Letters, 100(12): 561-570

<http://dx.doi.org/10.1080/09500839.2020.1820595>

N.B. When citing this work, cite the original published paper.

# Complete precipitate dissolution during adiabatic shear localisation in a Ni-based superalloy

Magnus Hörnqvist Colliander<sup>a</sup>, Gustav Sundell<sup>b</sup> and Mattias Thuvander<sup>a</sup>

<sup>a</sup>Department of Physics, Chalmers University of Technology, Gothenburg, Sweden; <sup>b</sup>Department of Chemistry and Chemical Engineering, Chalmers University of Technology, Gothenburg, Sweden

## ABSTRACT

Whereas microstructure evolution in adiabatic shear bands have been thoroughly studied, reports on the stability of hardening precipitates during shear localisation are scarce. We report an atomic scale investigation of solute distribution in adiabatic shear bands in a precipitation strengthened Ni-Fe-based superalloy, showing that the hardening particles are completely dissolved. Temperature estimations indicate that peak temperatures in the shear band above the solvus limits of the precipitates are not unrealistic, and thus diffusion-assisted transformations during the severe plastic deformation cannot be ruled out.

## ARTICLE HISTORY

Received 25 May 2020  
Accepted 7 August 2020


## KEYWORDS

Adiabatic shear bands; precipitation; atom probe tomography; superalloy

## 1. Introduction

The occurrence of adiabatic shear bands (ASBs), also known as white etching layers (WELs), in materials deformed at strain rates above around  $10 \text{ s}^{-1}$  has been known for decades [1], primarily through their high resistance to metallographic etching. The resistance to etching is a result of the formation of an ultra-fine grained (UFG) or nano-crystalline structure generally accepted to occur through a rotational dynamic recrystallisation (DRX) mechanism [2–4]. Although initially proposed to arise due to local adiabatic heating as a result of limited heat conduction during high strain-rate deformation [1], it is now known that DRX can precede, and indeed initiate, shear localisation, even in the absence of significant adiabatic heating through microstructural (rather than thermal) softening [5–7].

Whereas the onset and progression of DRX have been extensively investigated, only a very limited number of studies have been undertaken to characterise the microstructure in ASBs in precipitation hardened systems in detail. While dissolution of precipitates has been reported in ASBs in e.g. Al–Li [8–11], Al–Zn–Mg–Cu [12] and Mg–Zn–Zr alloys [13], these studies have relied on the

**CONTACT** Magnus Hörnqvist Colliander  magnus.colliander@chalmers.se

© 2020 The Author(s). Published by Informa UK Limited, trading as Taylor & Francis Group  
This is an Open Access article distributed under the terms of the Creative Commons Attribution-NonCommercial-NoDerivatives License (<http://creativecommons.org/licenses/by-nc-nd/4.0/>), which permits non-commercial re-use, distribution, and reproduction in any medium, provided the original work is properly cited, and is not altered, transformed, or built upon in any way.

absence of superlattice reflections in selected area electron diffraction (SAED) patterns, or in the case of [13] absence of visible precipitates in bright field transmission electron microscopy (TEM) images. Although the absence of superlattice reflections indicates the absence of ordered precipitates, it is not an unambiguous technique as it cannot detect disordered structures such as clusters. The severe plastic deformation could reduce the ordered precipitates to clusters, or such clusters could re-precipitate from a deformation induced solid solution state during post-deformation cooling, as the diffusion rates can be orders of magnitude higher in the severely deformed nano-structured state as compared to undeformed bulk material [14, 15]. Disordered clusters would not be visible in SAED diffraction, but could still have significant effects on both recrystallisation kinetics and mechanical properties of the ASB. Such effects must then be taken into account in predictive models, if the physics of the localisation process is to be captured. Accurate models of the shear band formation, as well as correct description of the constitutive behaviour of the material, are essential in order to further improve the understanding of many relevant dynamic deformation processes, such as ballistic impact and chip breaking during machining.

In the present study, we use high-resolution microstructural characterisation of ASBs formed during dynamic deformation of a precipitation hardened high-strength alloy, with high thermal stability of the secondary phases (solvus temperatures in the range 1133 to 1293 K (850 to 1020°C)), in order to unambiguously demonstrate the dissolution of the hardening precipitates within the shear bands on an atomic scale. This is made possible through atom probe tomography (APT), which has previously been used to reveal details of solute distribution in WELs in both steels [16] and Ni-based superalloys [17].

## 2. Experimental methods

The material is the Ni-Fe-based Alloy 718, with chemical composition (at.%, neglecting minor elements): Ni-20Cr-19Fe-3.2Nb-1.7Mo-1.2Ti-1.1Al. The material was heat treated to obtain a precipitation hardened state containing particles of  $\gamma'$  ( $L1_2$  structure, nominally  $Ni_3(Al,Ti)$ ) and  $\gamma''$  ( $D0_{22}$  structure, nominally  $Ni_3Nb$ ), typically around 20–30 nm in size (see, e.g. [17]). The precipitates provide substantial hardening to the fcc  $\gamma$  matrix, reaching room temperature yield strengths of around 1200 MPa. Additionally, the sub-solvus solution treatment left  $\delta$ -phase (orthorhombic  $Ni_3Nb$ ) present in the microstructure, inhibiting grain growth to maintain the grain size at around 10  $\mu\text{m}$ . Dynamic testing was performed at room temperature in a split Hopkinson pressure bar (SHPB, also referred to as Kolsky bar) rig, using a top-hat specimen [18], see Figure 1, specifically designed to produce shear localisation. Further details on the material, heat treatments and dynamic testing methods can be found elsewhere [19,20].

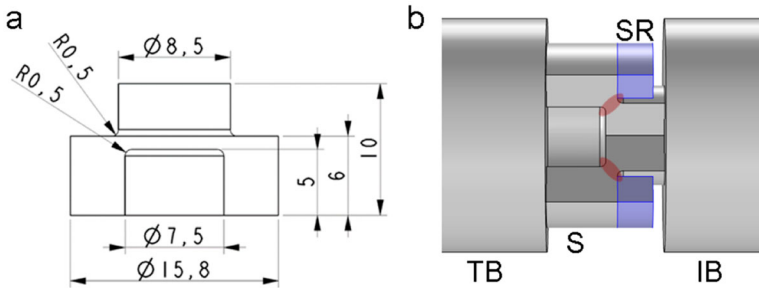


**Figure 1.** (a) Drawing of the top-hat specimen for dynamic shear testing (cross-section of rotational symmetric geometry). (b) 3D sketch of the central region of the experimental set-up, with cut-out to reveal internal details of the specimen (S). IB is the incident bar, TB is the transmission bar and SR is the stopper ring (in blue). The regions of localised shear are indicated by the red ellipses.

Scanning electron microscopy (SEM) using electron channelling contrast imaging (ECCI) was performed in an FEI Quanta 200 ESEM operated at 30 keV. Thin foils for TEM and specimens for APT were extracted using focused ion beam milling (FIB) in an FEI Versa3D dual beam instrument according to standard procedures. TEM was performed in an FEI Titan 80–300 operated at 300 keV. Transmission Kikuchi diffraction (TKD) investigations to reveal local texture were performed in a Leo Ultra 55 SEM at 20 keV, using a  $20^\circ$  specimen tilt. The Kikuchi patterns were recorded using an Oxford EBSD system with a NordLys II detector and analysed using MTEX [21]. For APT an IMAGO LEAP 3000X HR system was used and the specimens were tested at 70 K in laser pulsing mode (laser energy 0.4 nJ at 200 kHz) with a target evaporation rate of 3.0 %.

### 3. Results and discussion

After dynamic compression to a total displacement of 1 mm, pronounced shear localisation had occurred in the ligament of the top-hat specimens. Figure 2a shows the region of shear localisation in a sectioned specimen. The ASB itself is not visible in the optical micrograph, but clearly shown in the SEM micrograph insert and in Figure 2b. While the surrounding matrix shows distinct electron channelling contrast from the plastic deformation and presence of large  $\delta$ -phase particles, the contrast in the ASB indicates an UFG structure, in principle free of  $\delta$ . The transition zone is very narrow, and severe shearing and alignment of  $\delta$  particles can only be seen within a few  $\mu\text{m}$  from the matrix/ASB interface. The UFG structure was confirmed by TEM investigation of a lamellae extracted from the shear band (Figure 2c), revealing equiaxed grains in the size range 30–200 nm with a pronounced shear texture (shown by TKD on the same lamellae, Figure 2d). While SAED patterns were acquired from regions within the ASB (see insert in Figure 2c for an example), it was not possible to distinguish

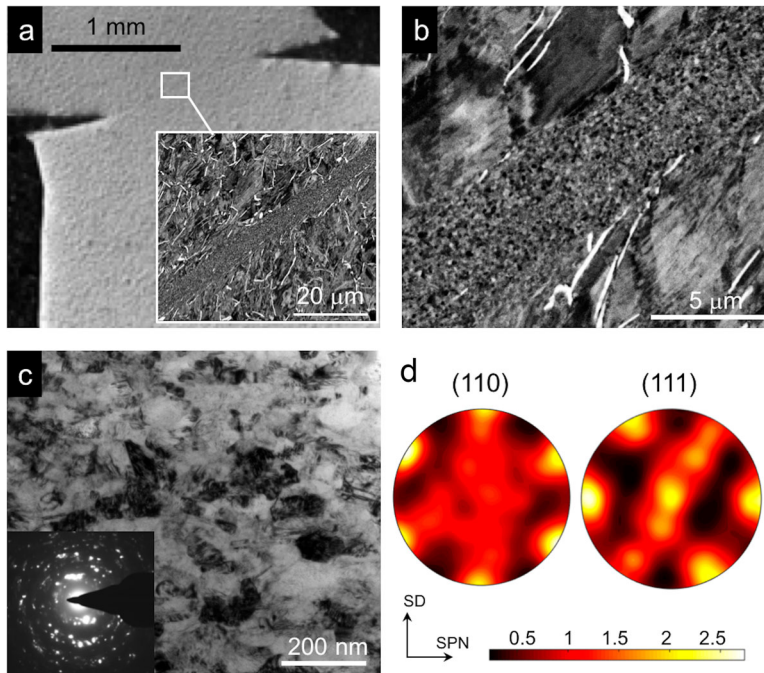


**Figure 2.** (a) Optical micrograph of the sheared ligament after 1 mm displacement. The ASB, extending between the two intrusion tips, is not visible in the image. Insert shows an SEM micrograph with a narrow (6–7  $\mu\text{m}$  wide) ASB with a very sharp interface to the surrounding material. Bright particles are  $\delta$ -phase. (b) Close-up of the shear band, suggesting an ultra-fine grained structure. (c) TEM bright field micrograph showing ultra-fine grains, with typical size in the order of 30–200 nm. The insert shows a typical SAED pattern from the ASB. (d) (011) and (111) pole figures from TKD investigations of the thin foil from (d). SPN denotes the shear plane normal, and SD is the shearing direction.

superlattice reflections from  $\gamma'/\gamma''$  phases in these patterns. This could be due to limited signal from reduced volume fractions and particle sizes, or even disordering, as a result of severe shearing, or absence of particles as a result of dissolution due to the thermal–mechanical history during deformation, as discussed previously.

Specimens for APT were extracted from the centre of the ASB in order to obtain sub-nm spatial distribution of solute elements in three dimensions. From the reconstructions, radial distribution functions (RDFs) for the main  $\gamma'$  and  $\gamma''$  forming elements (Al, Ti and Nb) were calculated. RDFs are obtained by taking each atom of a particular element, calculating the concentration in spherical shells with increasing radius around that atom, and summing over all atoms of that element. The result is normalised by the bulk average concentration, and an increase of the RDF above a value of unity is an indication of clustering of that element. Considering the expected counting errors, the RDFs for Al, Ti and Nb shown in Figure 3a do not reveal any significant deviations from unity, indicating absence of clustering. At very small distances, the

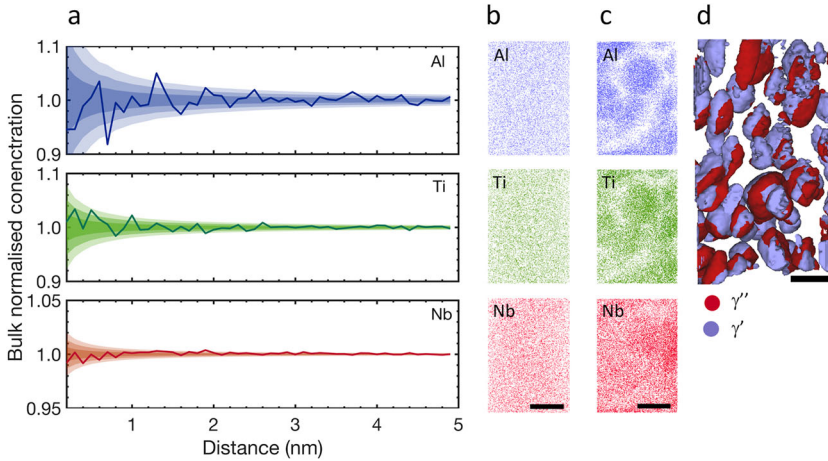


**Figure 3.** (a) Radial distribution functions for the main  $\gamma'$  and  $\gamma''$  forming elements (Al, Ti and Nb). The shaded areas correspond to  $\pm s$ ,  $\pm 2s$  and  $\pm 3s$ , where  $s = \sqrt{N_r/N_r}$ ,  $N_r$  being the number of ions counted in shell  $r$ . (b) Atom maps of Al, Ti and Nb (from top to bottom) from the APT reconstructions of the specimen from the ASB. (c) Same as (b) but from a specimen extracted from the undeformed bulk, for comparison. (d) Iso-surface reconstructions from a sample extracted from the undeformed bulk, showing the distribution of  $\gamma'$  (iso-concentration surface based on ratio  $(\text{Al}+\text{Ti})/(\text{Fe}+\text{Cr})$ , where the numerator contains  $\gamma'$  formers and the denominator species with strong preference for the  $\gamma$  matrix) and  $\gamma''$  (iso-concentration surfaces based on  $\text{Nb}/(\text{Fe}+\text{Cr})$  ratio). All scale bars are 20 nm.

number of counted atoms in each shell ( $N_r$ ) becomes small, leading to large random variations between adjacent shells, but no clear trends of increasing concentrations can be seen. Figure 3b shows atom maps of Al, Ti and Nb in a specimen taken from the ASB. The homogenous distribution of the precipitate forming elements is in stark contrast to the maps taken from the undeformed bulk material (Figure 3c), where Al- and Ti-rich  $\gamma'$  and Nb-rich  $\gamma''$  can be seen as dense atom clusters. The iso-concentration surfaces in Figure 3d clearly shows the presence of usually co-precipitated  $\gamma'$  and  $\gamma''$  particles in the size range 20–30 nm in the undeformed bulk. Considering the dense distribution in the bulk material, it is unlikely that the investigated volume (which is significantly larger than the selected slices shown in the associated atom maps in Figure 3c) is a randomly occurring volume without precipitates. The complete absence of particles or clustering in the ASB differs from previous observations in WELs in broached Alloy 718 [17]. While the microstructure in the WELs showed similar grain size and texture as in the present case, elongated nano-sized particles or cluster (rich in Al or Nb, but much smaller than the precipitates in the undeformed state), aligned in the broaching direction, were found. Although known to be very large, the strain levels during broaching are harder to estimate. The process is also much slower than in the present case, leading to a significant differences in thermomechanical history.

One potential reason for the differences between the broached WELs and the present ASBs discussed above could be a difference in peak temperature reached during deformation. Strain-induced dissolution of hardening precipitates has been reported during SPD, where the temperature rise is negligible [22–27]. Specifically for precipitation hardened superalloys, Zhang et al. showed that the  $\gamma'$  phase can actually undergo extensive plastic deformation during shearing, which allows shape changes involving elongations of the particles in the order of three to six times, without signs of reversion [28]. In the studies reporting particle dissolution in ASBs, on the other hand, diffusive phase transformation induced by adiabatic heating has been put forward as the dominating mechanism [8–11]. In order to further discuss the potential mechanisms behind the observed precipitate reversion in the present case, it is necessary to estimate the local deformation conditions in the ASB. Due to the complex specimen geometry, the standard formulas for the calculation of stress, strain and strain rate during SHPB testing are not applicable. However, the global force–displacement history is available and can be used to approximately assess the local condition from geometrical considerations [29]. The force–displacement curve (Figure 4a) shows the typical behaviour associated with shear localisation, with a sudden drop in the force occurring at displacements

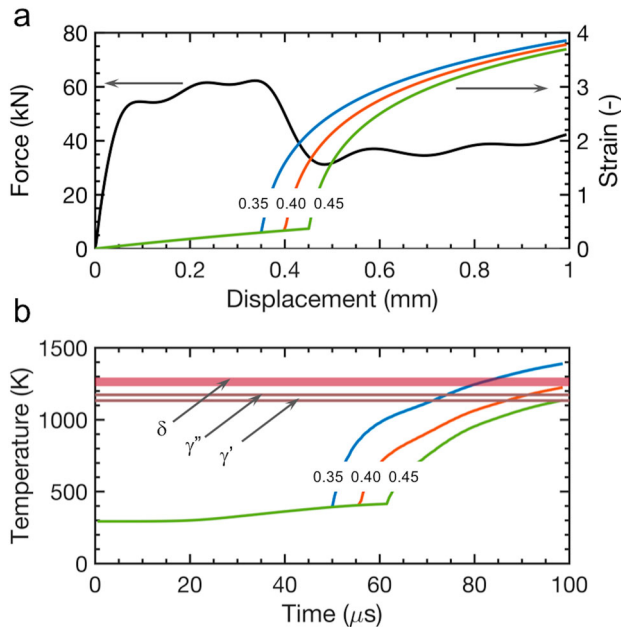


**Figure 4.** (a) Measured global force–displacement curve (left axis) and calculated strain–displacement curves for different assumed ASB initiation points corresponding to a displacement of 0.35, 0.40 and 0.45 mm (right axis). (b) Calculated temperature evolution in the ASB as a function of time for the different assumed initiation points. The temperature marked correspond to approximate solvus temperatures of the secondary phases:  $\gamma' \approx 1133$  K (850°C),  $\gamma'' \approx 1173$  K (900°C) and  $\delta \approx 1233$ –1293 K (950–1020°C).



between 0.35 and 0.45 mm. Such a drop is generally considered to arise from the locally reduced flow stress in the ASB, and the correlation between these two phenomena (ASB formation and stress drop) for the material in question has been demonstrated in previous studies [19, 20]. The shear strain in the deforming ligament is given by  $\Gamma = \Delta/w$ , where  $\Delta$  is the displacement and  $w$  is the width of the sheared region. Before the formation of the ASB, the whole ligament is deformed, and  $w$  corresponds to the difference between the radius of the top and bottom parts of the specimen. Upon shear localisation the strain is concentrated to the band, and  $w$  corresponds to the ASB width ( $\approx 7 \mu\text{m}$ , as measured from SEM images, see Figure 2). Thus, here we find the shear strain at time  $t_i$  as the sum over all previous displacement increments divided by the respective  $w$ , corresponding to ligament width for points before strain localisation, and ASB width (assumed to remain constant at  $7 \mu\text{m}$  throughout the test) for subsequent points:

$$\Gamma(t_i) = \sum_{k=0}^i \frac{\Delta_k}{w_k}. \quad (1)$$

The true strain is given by

$$\epsilon(t_i) = \ln \sqrt{1 + \Gamma(t_i) + \frac{\Gamma(t_i)^2}{2}}, \quad (2)$$

and the shear stress in the ligament or ASB is given by

$$\tau(t_i) = \frac{P_\theta(t_i)}{\pi l d_{av}}, \quad (3)$$

where  $P_\theta(t_i)$  is the resolved force component in the shear plane at time  $t_i$ ,  $d_{av}$  is the average diameter of the ligament and  $l$  is the length of the ligament (distance between inner and outer fillet radius). The temperature evolution in the ASB is then obtained by numerical integration of the thermal balance equation (under the assumption of adiabatic conditions and neglecting thermo-elastic effects) as

$$T(t_i) = T_0 + \frac{\beta}{\rho C_p} \sum_{k=0}^i \sigma_k \Delta \epsilon_k \quad (4)$$

with  $\beta = 0.9$ ,  $C_p = 435 \text{ J}\cdot\text{kg}^{-1}\cdot\text{K}^{-1}$ ,  $\rho = 8.22 \text{ g}\cdot\text{cm}^{-2}$  (the temperature dependence of these parameters was neglected) and  $\sigma = 1.25\tau$  from geometric consideration of the offset between inner and outer radii.

The resulting calculated strain evolution in the ASB is shown in Figure 4a as a function of displacement. As the exact transition point from deformation of the entire ligament to localisation in the ASB and the kinetics of that transition are not known, the calculations were performed for three different assumed



localisation points,  $\Delta=0.35, 0.40$  and  $0.45$  mm. These points correspond to the start, middle and end of the force drop. Note that the final true strain at 1 mm displacement estimated from the post-test measured shear displacement of the ligament was 4.13, which agrees well with the calculated strain levels. Figure 4b shows the calculated temperature evolution in the ASB as a function of time. The final temperature depends strongly on the displacement at which the deformation is assumed to transfer from the entire ligament to the ASB, with maximum temperatures of 1391 K (1118°C), 1226 K (953°C) and 1137 K (864°C) being reached for assumed localisation at 0.35, 0.40 and 0.45 mm, respectively. These temperatures can then be compared to the different solvus temperatures of the secondary phases: 1133 K (850°C) for  $\gamma'$ , 1173 K (900°C) for  $\gamma''$ , and 1233–1293 K (950–1020°C) for  $\delta$ .

In addition to the higher maximum temperature (faster diffusion), earlier localisation also causes temperatures in the solvus range to be reached earlier in the tests, allowing more time for diffusional transformations to occur. There is also an additional time spent at elevated temperatures during the period of cooling when the deformation stopped. As the level of deformation surrounding the ASB is very small [19], it will remain at temperatures very close to ambient, acting to effectively quench the ASB when the test is stopped. Approximate 1D simulations give cooling times to temperatures below the  $\gamma'$  solvus of less than a  $\mu\text{s}$ , and to below 773 K (500°C), where any diffusion will be negligible, in the order of  $5 \mu\text{s}$ .

Whereas such an analysis clearly indicates that temperature excursions into the regime where diffusion assisted particle dissolution *could* occur, more thorough simulations and *in situ* experiments (e.g. high-rate acquisition scattering techniques at synchrotrons) are necessary to clarify the details of the deformation and temperature history. Additionally, cryogenic dynamic shear testing, which has been used previously to demonstrate the need for a peak temperature above the precipitate solvus limit to dissolve the secondary phases in ASBs in Al–Li alloys [8], could be used to lower peak temperatures into the sub-solvus regime in order to separate the effects of strain and temperature. Another important factor to consider in a more detailed analysis is the temperature and material dependence of the Taylor–Quinney coefficient ( $\beta$  in Equation 4), which will drastically affect the predicted temperature history. Although a value of  $\beta = 0.9$  is commonly assumed, a thorough experimental study has recently reported values of  $\beta$  between 0.2 and 0.9, depending on material and test conditions [30].

#### 4. Conclusion

In summary, we have unambiguously demonstrated that the particles in a high-strength, high-temperature, precipitation strengthened Ni–Fe based superalloy can be completely dissolved in ASBs formed during dynamic deformation.

We have also shown that temperature excursions into the super-solvus regime is not unrealistic, and that diffusion assisted dissolution, in conjunction with mechanical scrambling, cannot be ruled out.

## Acknowledgments

The authors would like to acknowledge Prof. Christer Persson and Dr. Joakim Johansson for supplying the tested top-hat specimen, Dr. Haiping Lai and Dr. Anand H. S. Iyer for technical assistance with TEM and SEM investigations. Prof. Kenneth Vecchio at University of California San Diego is acknowledged for access to SHPB equipment and technical assistance during testing.

## Disclosure statement

No potential conflict of interest was reported by the authors.

## Funding

The SHPB testing was financially supported by the Swedish Innovation Agency (VINNOVA) and GKN Aerospace in collaboration, through the National Aerospace Research Program (NFFP, grant number 2010-01236).

## References

- [1] C. Zener and J. Hollomon, *J. Appl. Phys.* 15 (1944) p.22.
- [2] J. Hines, K. Vecchio and M. Meyers, *Metal. Mater. Trans. A* 29 (1998) p.191.
- [3] M. Meyers, V. Nesterenko, J. LaSilva and Q. Xue, *Mater. Sci. Eng. A* 317 (2001) p.204.
- [4] Y. Xu, J. Zhang, Y. Bai and M. Meyers, *Metal. Mater. Trans. A* 39 (2008) p.811.
- [5] D. Rittel, P. Landau and A. Venkert, *Phys. Rev. Lett.* 101 (2008) p.165501.
- [6] D. Rittel, *J. Phys. D Appl. Phys.* 42 (2009) p.214009.
- [7] P. Landau, S. Osovski, A. Venkert, V. Gärtnerová and D. Rittel, *Sci. Rep.* 6 (2016) p.37226.
- [8] R. Chen and K. Vecchio, *J. Phys. IV* 4 (1994) p.C8.
- [9] Y. Xu, W. Zhong, Y. Chen, L. Shen, Q. Liu, Y. Bai and M. Meyers, *Mater. Sci. Eng. A* 299 (2001) p.287.
- [10] Y. Yang, Y. Chen, L. Jiang, M. Li, Q. Zhang and T. Tang, *Appl. Phys. A Mater. Process.* 121 (2015) p.1277.
- [11] Y. Yang, S. Luo, H. Hu, T. Tang and Q. Zhang, *J. Mater. Res.* 31 (2016) p.1220.
- [12] H. He, X. Wu, C. Sun and L. Li, *Mater. Sci. Eng. A* 745 (2019) p.429.
- [13] L. Jiang, Y. Yang, Z. Wang and H. Hu, *Mater. Sci. Eng. A* 711 (2018) p.317.
- [14] Y. Huang, J. Robson and P. Pragnell, *Acta Mater.* 58 (2010) p.1643.
- [15] L. Jiang, J. Li, P. Cheng, G. Liu, R. Wang, B. Chen, J. Zhang, J. Sun, M. Yang and G. Yang, *Mater. Sci. Eng. A* 607 (2014) p.596.
- [16] S. Hosseini, M. Thuvander, U. Klement, G. Sundell and K. Rytberg, *Acta Mater.* 130 (2017) p.155.

- [17] Z. Chen, M. Hörnqvist Colliander, G. Sundell, R. Peng, J. Zhou, S. Johansson and J. Moverare, *Mater. Sci. Eng. A* 684 (2017) p.373.
- [18] L. Meyer and S. Manwaring, *Metallurgical applications of shock-wave and high-strain-rate phenomena*, in *Critical Adiabatic Shear strength of Low Alloyed Steel Under Compressive Loading*, Marcel Dekker, New York, NY (1986), p.657.
- [19] J. Johansson, C. Persson, H. Lai and M. Hörnqvist Colliander, *Mater. Sci. Eng. A* 662 (2016) p.363.
- [20] J. Johansson, C. Persson, G. Testa, A. Ruggiero, N. Bonora and M. Hörnqvist Colliander, *Mech. Mater.* 109 (2017) p.88.
- [21] R.H.F. Bachmann and H. Schaeben, *Sol. State Phen* 60 (2010) p.63.
- [22] M. Murayama and K. Horita Z. Hono, *Acta. Mater.* 49 (2001) p.21.
- [23] K. Oh-ishi, Y. Hashi, A. Sadakata, S. Kaneko, Z. Horita and T. Langdon, *Mater. Sci. Forum* 396–402 (2002) p.333.
- [24] M. Cabibbo, E. Evangelista and M. Vedani, *Metal. Mater. Trans. A* 36 (2005) p.1353.
- [25] Z. Liu, S. Bai, X. Zhou and Y. Gu, *Mater. Sci. Eng. A* 528 (2011) p.2217.
- [26] S. Mukhtarov and X. Sauvage, *Mater. Sci. Forum* 683 (2011) p.127.
- [27] X. Sauvage and S. Mukhtarov, *Microstructure evolution of a multiphase superalloy processed by severe plastic deformation*, IOP Conference Series: Materials Science and Engineering 2014(63), p. 012173.
- [28] G.Y.P. Zhang L. Ma and X. Song, *Phil. Mag. Lett.* 96 (2016) p.19.
- [29] U. Andrade, M. Meyers, K. Vecchio and A. Chokshi, *Acta Mater. Metal.* 42 (1994) p.3183.
- [30] D. Rittel, L. Zhang and S. Osovski, *J. Mech. Phys. Solids.* 107 (2017) p.96.